Published in : Microscopy and Microanalysis (2009), vol.15, pp. 384-394
Status: Postprint (Author's version)

X-Ray Microtomography Studies of Tannin-Derived Organic and Carbon Foams

G. Tondi,[1,5] S. Blacher,[2] A. Léonard,[2] A. Pizzi,[1] V. Fierro,[3] J.M. Leban,[4] and A. Celzard[3,5]

[1]*Nancy University, ENSTIB-LERMAB, 27 rue du Merle Blanc, BP 1041, 88051 Epinal cedex 9, France*
[2]*University of Liège, Laboratory of Chemical Engineering, Department of Applied Chemistry, F.RS.-FNRS, B6C - Sart Tilman, 4000 Liège, Belgium*
[3]*Nancy University, Institut Jean Lamour - UMR CNRS 7198, Département Chimie et Physique des Solides et des Surfaces, Faculté des Sciences & Techniques, BP 239, 54506 Vandœuvre lès Nancy cedex, France*
[4]*1NRA, LERFOB - UMR 1092, Equipe de Recherche Qualité du Bois, 54280 Champenoux, France*
[5]*Nancy University, Institut Jean Lamour - UMR CNRS 7198, Département Chimie et Physique des Solides et des Surfaces, ENST1B, 27 rue du Merle Blanc, BP 1041, 88051 Epinal cedex 9, France*

Abstract: Tannin-based rigid foams of different bulk densities and their carbonized counterparts were investigated for the first time by X-ray microtomography. This method allowed acquisition of three-dimensional pictures of such highly porous materials. Through mathematical treatment of the images, extremely useful physical characteristics such as porosity, fraction of open cells, connectivity, tortuosity, and pore-size distribution were determined as a function of the foam's density. The obtained information was compared with independent data derived from pycnometry measurements and scanning electron microscope image analysis. The agreement was shown to be acceptable in the limit of the accuracy of the laboratory microtomograph (4 μm). Moreover, recalculating properties like permeability were shown to be quite possible based on the results of standard microtomography data.

Key words: rigid foam, microtomography, image analysis, permeability, tortuosity, porosity, tannin, carbon

INTRODUCTION

Solid foams are versatile materials of high technological interest combining a number of valuable—and sometimes very different—properties (Gibson & Ashby, 1997). For example, polyurethane foams are elastic and heat insulating, whereas carbon foams are hard and may be used as heat exchangers. For a given composition of the foam, physical properties like permeability, thermal conductivity, and mechanical and radiative behaviors strongly depend on pore structure: pore-size distribution, connectivity, and tortuosity of pores. Additional characteristics such as bulk density and surface area depend on linear pore density and average thickness of pore walls. Hence, the texture characterization of these highly porous materials is a major issue in relation with their potential applications.

The present study deals with a new kind of foam of vegetable origin, derived from tannins. The interest for such "green" materials, based at 95% on natural resources and first developed by Pizzi in 1994 (Meikleham & Pizzi, 1994), has been renewed in the recent years. Their properties were investigated in detail (Tondi & Pizzi, 2008), and applications were suggested as absorbers for heavy metal removal (Tondi et al., 2008a) and as thermal insulating materials (Tondi et al., 2008b). The investigation of their carbonaceous counterparts, obtained by pyrolysis of tannin-based organic foams, has just begun (Tondi et al., 2009). A detailed study of the topology of pores in organic and carbonized foams is the subject of this article.

Mercury porosimetry is traditionally used to characterize this kind of foam material. However, the use of this technique is not appropriate in the present case because mercury porosimetry is limited to a maximum pore size of 75 μm. Depending on the parameters used in the foaming process, the porosity can be so open that mercury would not infiltrate the sample but would flow through the pore structure. Moreover, it has been shown that some materials, like anisotropic poly(L-lactide-co-ε-caprolactone) foams generated by freeze-drying (Tija & Moghe, 1998; Maquet et al., 2003) as well as biodegradable scaffolds obtained with supercritical CO_2 as the foaming agent (Léonard et al., 2008*a*), shrink under the high pressure required for Hg intrusion.

Recently, various groups used X-ray microtomography coupled with image analysis to characterize the morphological structure of highly porous materials of different origins (Blacher et al., 2004; Trater et al., 2005; Babin et al., 2007;

Maire et al., 2007; van Lenthe et al., 2007; Léonard et al., 2008b; Viot et al., 2008). X-ray microtomography enabled visualization of the internal structure of the investigated object in a nondestructive way. Analyses of the

resulting two-dimensional (2D) or three-dimensional (3D) images allowed quantification and characterization of the observed structure.

In these studies, this technique was applied to characterize the influence of the synthesis conditions and of the subsequent carbonization step on the 3D structure of tannin-based rigid foams. The results are compared with independent data derived from scanning electron microscopy, bulk density, and helium pycnometry measurements.

MATERIALS AND METHODS

Synthesis of Organic Foams

Tannin extracts are commercial materials of vegetable origins. They are mainly composed of condensed flavonoids, which are able to undergo the same reaction as that of phenol with formaldehyde or other aldehydes, although with a much lower reactivity (Pizzi, 1994). Typical self-blowing tannin-based rigid foams were produced according to the following method (Tondi & Pizzi, 2008). 10.4 g of furfuryl alcohol (strengthener), 7.4 g of formaldehyde 37% water solution (cross-linking agent), and 6.0 g of water (solvent) were mixed with 30 g of mimosa tannin bark extract *(Acacia mearnsii* formerly *mollissima*, de Wildt) under mechanical stirring. When the viscous solution was homogeneous, various amounts of diethyl ether (DEE) (foaming agent): from 2.0 to 4.0 g were added and mixed to the bulk to obtain different densities for the final foam. Then, 12.0 g of 65% toluene-4-sulphonic acid water solution (catalyst) was mixed allowing the polymerization reaction to start. The mixed solution was then immediately discharged in a 6 × 6 cm square based plastic (polyethylene) box.

The exothermic reaction, due to both the self-polymerization of furfuryl alcohol and by its reaction with tannins in acidic conditions, took place in 60-90 s after catalyst addition, and the temperature rose to about 40°C. In these conditions, the heat thus generated produced the evaporation of the DEE and hence the foaming. Concurrently, cross-linking occurred so the foam hardened once the porosity was well developed and before the cells collapsed. The final density of the materials was tuned through the initial amount of foaming agent. The resultant foams may replace phenol-formaldehyde foams in most of applications because of their similar physical properties.

After foaming, each material was removed from its box and left to harden, age, and lose its solvent for 2-3 days. The external parts over a thickness of a few millimeters beneath the skin were systematically eliminated. Due to the vertical rising of the gas during foaming, the foams formed orthotropic materials. They indeed present slightly elongated cells in the direction of cell growth, whereas the pores appear to be isotropic when observed in the orthogonal plane. The microtomographic investigation was carried out according to the direction of growth only. The name DEEx of the tannin foam samples scanned in the X-ray microtomograph, their corresponding bulk density and dimensions are given in Table 1. X indicates the mass (g) of DEE used in the composition; the higher the X value, the higher the amount of foaming agent, and hence the lower the corresponding density (see below).

Table 1. : *Denomination and the Corresponding Bulk Density and Dimensions for Each Sample.*

Sample Name	**Bulk Density (gcm^{-3})**	**Dimensions (mm)**
Organic foams		
DEE2	0.0928	8×4×4
DEE3	0.0625	7×5×4
DEE4	0.0495	7×5×5
Carbon foams		
DEE2C	0.1072	8×5×5
DEE3C	0.0733	7×4×4
DEE4C	0.0623	7×4×4

Published in : Microscopy and Microanalysis (2009), vol.15, pp. 384-394
Status: Postprint (Author's version)

Synthesis of Carbon Foams

Carbon foams derived from organic materials were obtained by controlled pyrolysis of the latter. A previous study (Tondi et al., 2009) showed that shrinkage is very important with the sample volume being divided by a factor of about 2; however, no cracks appear, and the pore structure is fully maintained while the resin is gradually transformed into disordered (glass-like) carbon.

Three cubic foam samples of side 15 to 20 mm of different densities were put inside a quartz boat installed in the middle of a quartz tube continuously flushed with high-purity nitrogen (typical flow rate: 25 mL min^{-1}). The tube was heated by an electric furnace from room temperature up to 900°C at 5°C/min. The final temperature was held for 2 h, then the furnace was switched off, and the samples were allowed to cool down to room temperature under nitrogen flow.

The name of the resultant carbon samples (DEExC), their bulk density and dimensions are given in Table 1. Since the materials submitted to pyrolysis present rather similar values of weight loss and volume reduction (Tondi et al., 2009), their final bulk density is close to that of the initial organic foams.

X-Ray Microtomography

X-ray tomography is a nondestructive imaging technique that allows access to the internal structure of the investigated object. This technique, based upon the local variation of the X-ray attenuation coefficient of the object located along the X-ray path, is similar to the one used in a medical scanner. During tomography investigation, an X-ray beam is sent to the sample, and the transmitted beam is recorded by a detector. According to the Beer-Lambert's law, the transmitted intensity is related to the integral of the X-ray attenuation coefficient along the beam path. This coefficient depends on the density and the composition (through the atomic number) of the material, and on the energy of the incident beam (Kak & Slaney, 1988). Projections, or radiographies, are recorded for several angular positions by rotating the sample between 0 and 180 deg. Then, a back-projection algorithm is used to reconstruct 2D or 3D images, depending on the method used. In the case of 2D images, each pixel has a gray level value corresponding to the local X-ray attenuation coefficient.

In this work, the "Skyscan-1172 high-resolution desktop micro-CT system" (Skyscan, Kontich, Belgium) was used. By contrast with a classical medical scanner, the source and the detector were fixed, while the sample was rotated during the measurement. The cone beam source operated at 60 kV and 167 μA. The detector was a 2D, 1,048 × 4,000 pixels, 16-bit X-ray camera. The distance source-object-camera was adjusted to produce images with a pixel size of 4 or 5 μm, depending on the sample. The rotation step was fixed at 0.4 deg. Concerning radiography recording, the frame averaging was set to 16 in order to increase the signal-to-noise ratio. For each sample, the resulting acquisition time was close to 1 h.

Two-dimensional cross sections of the sample foam were reconstructed using a Feldcamp back-projection algorithm provided with the X-ray microtomograph. For each sample, 500 cross sections of 500 × 500 pixels, separated by 4 or 5 µm, were reconstructed. The 3D images of the samples were then built by stacking the 500 averaged cross sections.

Image Analysis

The 3D image of any foam material is formed by two phases: pores at low gray levels (dark voxels) and the cell walls at high gray levels (bright voxels). Before any measurement, images were processed as follows: a low-pass filter was applied to eliminate noise and then the "top-hat" filter (Soille, 1999) to highlight the local maxima. After that, images were binarized by assigning a value of 1 to all voxels with intensity below a given threshold (pores) and a value of 0 to the others (cell walls). Practically, an automatic threshold technique, which consists in selecting the threshold that maximizes the global average contrast of edges (Kohler, 1981), was applied on the 3D gray level images.

The above-described way of processing the images results from a compromise between oversegmentation and persistence of noise and needs to be explained. For the sake of clearness, the discussion is made on the basis of 2D cross-section images, but the entire image processing method described below can be also applied to 3D images. A typical cross section of the studied foam is presented in Figure la. It corresponds to a gray level image in which pores are bright (with intensities close to 255) and the walls, which absorb X-rays, are dark (with intensities close to 0). To increase the global contrast of the image, the histogram equalization transformation (Russ, 1999) was applied (Fig. lb). This transformation allows detecting the thinner walls as well as a

background random noise. Indeed, X-ray signals are inherently noisy because both their generation and scattering are stochastic processes. Moreover, the detector and its amplification electronics contribute to additional noise.

The classical problem when processing this kind of image is that noise features have the same gray level intensity and/or the geometrical size that the objects under study have. As a consequence, the process used to remove noise features leads to the simultaneous removal of the thinner walls. This is clearly shown in Figure 1c in which, after filtering and binarization using the adopted method described at the beginning of this section with the appropriate parameters, noise was completely removed as well as some walls or parts of walls (see arrows in Fig. 1c).

Mathematical morphology provides a powerful tool to recover the walls of the porous structure. It consists in the application of the watershed segmentation (Soille, 1999). This methodology is usually used to separate artificially connected or overlapping convex features in an image. Figure Id shows the resulting image obtained after application of the watershed transformation to Figure 1c. For each portion of a pore that does not deviate too much from a disk, a segmentation line was produced by the algorithm, giving rise to a "cellular" pore structure. A comparison among Figures 1b, 1c, and 1d indicates that some walls or portion of walls that were removed by the noise filtering were recovered. On the other hand, due to the roundness of some portion of pores, new walls were generated (see arrows in Fig. 1b,d). Perhaps these new walls exist, but they were not detectable at the observed device resolution and consequently must not be taken into account. Indeed, the existence of these walls would imply that porosity is completely closed, which is in contradiction with the physical measurements and the foaming process (see below). Moreover, taking these walls into account would also lead to a pore-size distribution shifted toward smaller values. Then, since a complete noise filtering leads to the removal of walls, and since recovering the walls leads to an oversegmentation, a compromise was made consisting of performing an incomplete filtering to preserve walls with the potential drawback of keeping some noise in the images. The image obtained using this criterion is shown in Figure le. It must be noticed that, due to the random character of noise, it would not significantly affect pore-size distribution and tortuosity measurements. However, the total porosity is expected to be lower than that obtained by physical measurements.

From the 3D binary images obtained with the above-described processing, the following parameters were measured:

1. total porosity, defined as the fraction of voxels of the image that belongs to the pores
2. closed porosity, defined as the fraction of voxels of the image that belongs to the pores that are not connected to the exterior of the foam
3. opening size granulometry: since foams present a continuous and rather disordered pore structure, a standard granulometry measurement could not be applied. Then, for quantifying the void size distribution, the opening size distribution (Soille, 1999) was calculated. This method allows assigning a size to both continuous and individual particles.
4. tortuosity, defined as the ratio between the straight-line distance between two pores and the shortest distance between them that lies entirely within the pore space (Clennell, 1997). The practical method to measure tortuosity in 3D objects is described in detail in Gommes et al. (2009).

Image processing and measurements, as well as statistical analyses, were performed using Matlab software 7.1 with the image analysis, SDC morphology, and statistic toolboxes. As distribution curves calculated in this work were skewed and nonnormally distributed, usual descriptive statistical parameters such as mean and standard deviation were not relevant. To give an idea of centrality and spread of this kind of empirical distribution, percentiles are usually used. Percentiles provide an estimation of the proportion of data that fall above a given value, i.e., Xth percentile means that at most X% of values are less than this value. In this work we determined, for each calculated distribution, X_{25}, X_{50}, and X_{75} percentiles. It is worth noting that X_{50} corresponds to the median of the distribution.

Scanning Electron Microscope Observations

Only carbon foams, completely stable in vacuum, were observed by scanning electron microscope (SEM) (organic foams would have release water in the same conditions and would decompose under the electron beam). Small samples (a few millimeters long) were glued to the sample holder with varnish and carbon-coated for ensuring a good electrical contact with the sample holder. The main intrinsic characteristics of the carbon foam, cell structure and average pore size, were evaluated by SEM observation (Hitachi S 4800). For each material, a number of SEM images of their surface were considered, in which the dimensions of several tens of cells were systematically measured. Average cell diameters were thus obtained.

Figure 1. *(a) Original gray level image; (b) image after histogram equalization; (c) binary image after noise removal by filtering; (d) binary image after wall recovery using watershed segmentation; (e) binary image after the "compromise" methodology. Arrows indicate the occurrence/removal of pore walls, depending on the treatment applied to the image (see text).*

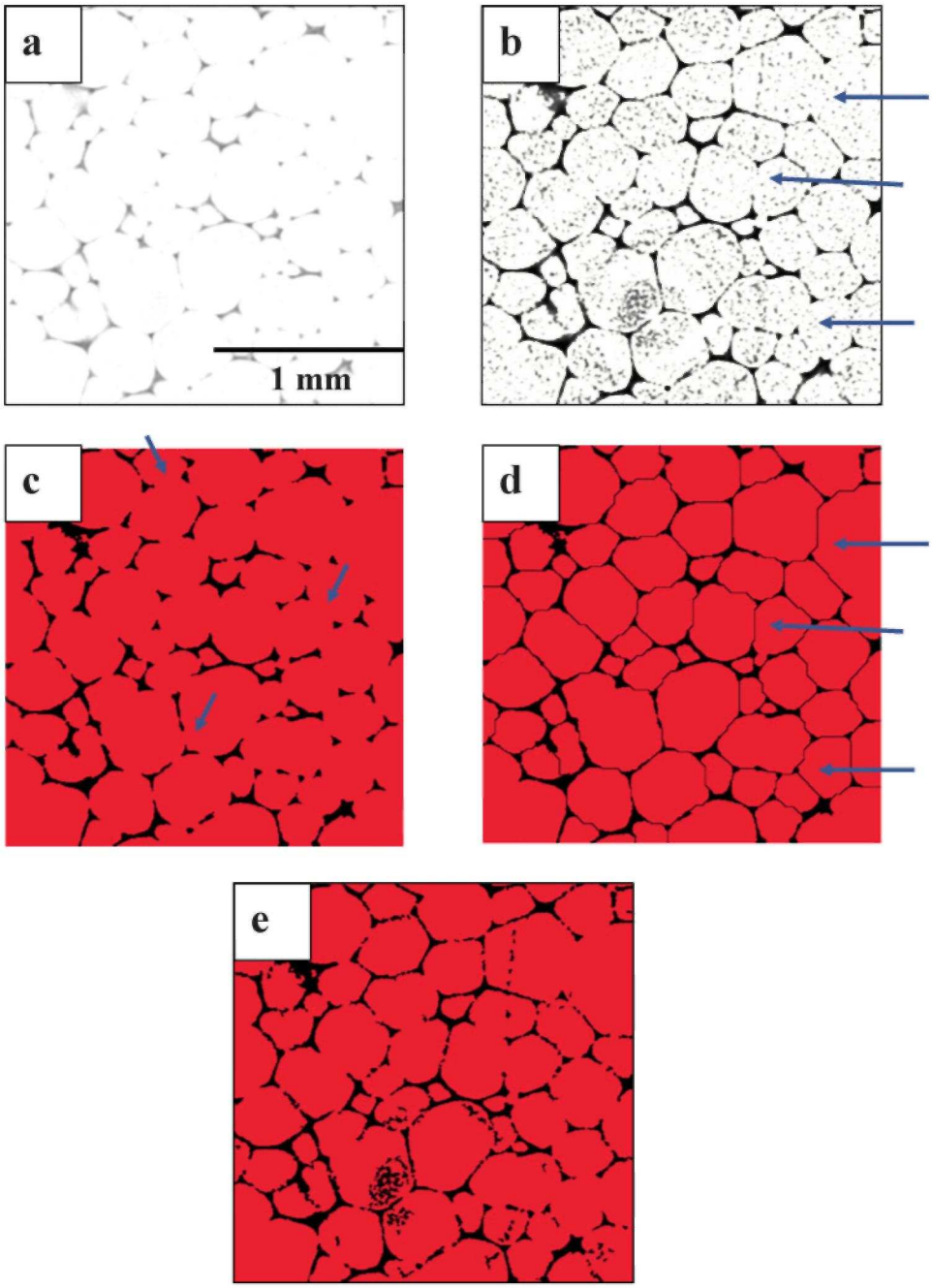

Porosity Determination

Two densities can be defined on a porous material: the bulk density (given in Table 1) is defined as the mass of material divided by the total volume it occupies, whereas the skeletal density, sometimes called true density, is that of the solid from which the considered material is made. The total porosity Φ was calculated according to equation (1):

$$\Phi = 1 - \frac{\rho_b}{\rho_s}, \qquad (1)$$

where ρ_h and ρ_s are the bulk and true skeletal densities of the foam, respectively. Helium pycnometry was carried out on several foams in a lab-made apparatus, and the "apparent" skeletal density (i.e., not taking closed pores into account) was measured accordingly. Once the material was finely crushed in a mortar, the true skeletal density could be determined. The fraction of open cells was deduced by the application of equation (2):

$$\%\ \text{open cell} = \frac{\text{skeletal density of the foam}}{\text{skeletal density of the pulverized foam}} \times 100. \qquad (2)$$

RESULTS AND DISCUSSION

Qualitative Approach

Typical cross sections and 3D reconstructed images of DEE2, DEE3, and DEE4 (Table 1) before and after carbonization are shown in Figures 2 and 3, respectively. For the sake of clearness, pores are represented in the form of solid bodies separated by thin pore walls. Such a complementary way of presenting the structure is sometimes easier for visualizing the porosity and its connectivity.

Examination of these pictures and many others (not shown) lead to the following features concerning organic foams (see Fig. 2):

1. The cell walls are increasingly thinner from DEE2 to DEE4.
2. The average diameter of the windows connecting the cells with each other increases from DEE2 to DEE4.
3. Anisotropy increases from DEE2 to DEE4, through the gradual elongation of the cells along one direction.
4. At first sight, the pore-size distribution looks homogeneous in each foam, although a few defects in the form of irregular big cells may sometimes be observed, especially for DEE2.

The first three observed characteristics result from the synthesis conditions of the foams. The amount of foaming agent (diethyl ether) increases from DEE2 to DEE3 and DEE4, being 2.0, 3.0, and 4.0 g in composition given above, respectively. Consequently, the higher amount of gas generated from DEE2 to DEE4 simultaneously explains the easier bubble growth and rising (hence the increasing anisotropy), the higher pore volume (hence the lower density and thus the bigger cell diameter and the corresponding thinner cell walls), and the expected higher cell connectivity through the higher window diameter. The fourth observation will be discussed in the quantitative approach section.

The aforementioned features can also apply to carbon foams (see Fig. 3). In a previous work (Tondi et al., 2009), it was shown that the shrinkage occurring during pyrolysis was homogeneous; the pore structure is thus expected to be the same as that of the organic foams but with smaller cells and smaller windows. This is what is observed when the images of Figure 2a-c are compared to images of Figure 3a-c, respectively.

Quantitative Approach

Three-dimensional image analysis allows quantification of the influence of synthesis conditions on the foam structure, before and after carbonization. Total and closed porosity, tortuosity, and statistical parameters corresponding to the pore-size distribution were calculated according to the protocol described above and are presented in Table 2. Pore-size distributions corresponding to the investigated samples are presented in Figure 4.

Published in : Microscopy and Microanalysis (2009), vol.15, pp. 384-394
Status: Postprint (Author's version)

Figure 2. *(a-c) Typical cross sections and (d-f) 3D X-ray tomography rendering of organic foams DEE2, DEE3, and DEE4, respectively.*

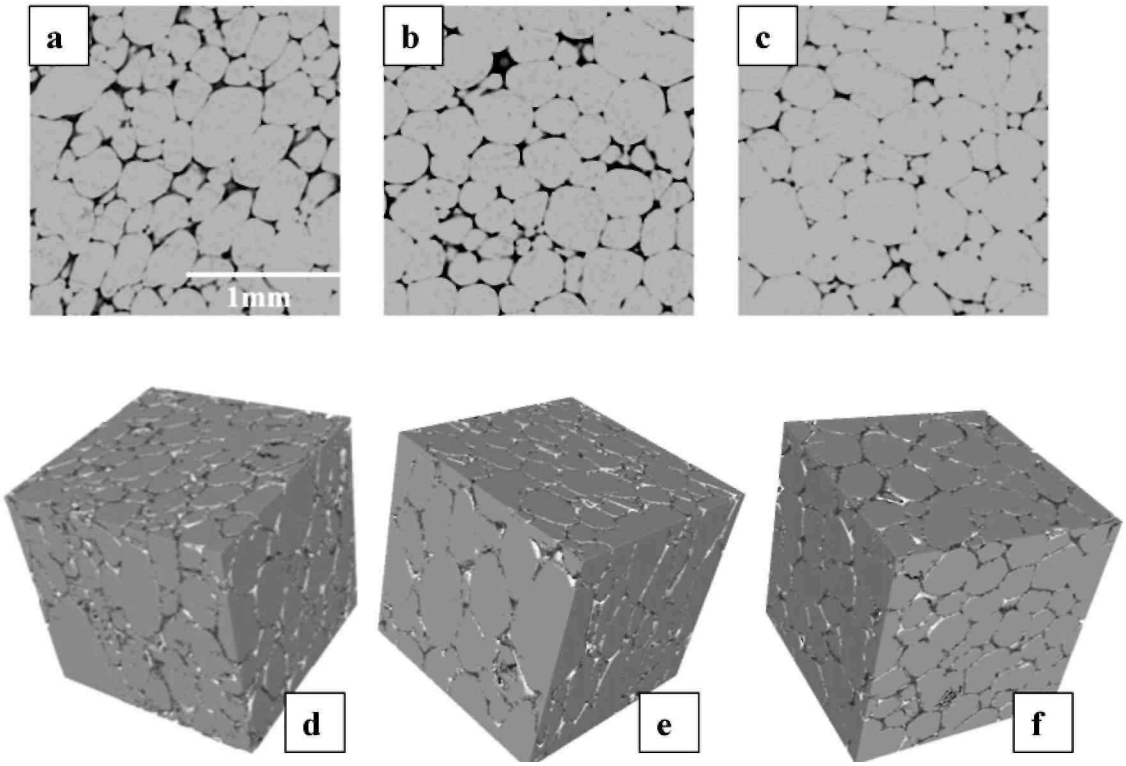

Figure 3. *Same as Figure 2, but for carbon foams DEE2C, DEE3C, and DEE4C, respectively.*

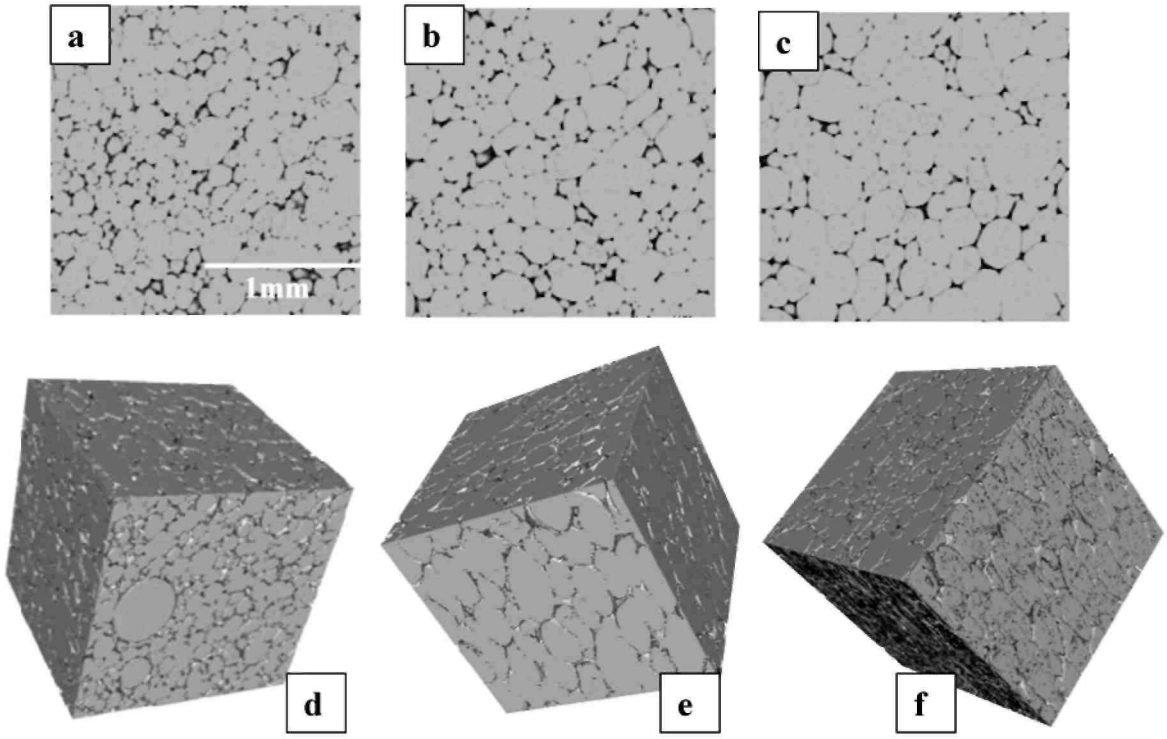

Table 2. *Pore Structure Parameters Derived from the Quantitative Analysis of X-Ray Microtomography Pictures.**

Sample	Total Porosity (±0.005) (%)	Closed Porosity (±0.005) (%)	Connectivity	Tortuosity	Pore-Size Distribution			
					X_{25} (μm)	X_{50} (Median) (μm)	X_{75} (μm)	Mean (μm)
DEE2	82	0.02	1.0	1.21 ± 0.03	82.74	141.83	220.63	161 ± 98
DEE3	87	0.01	1.0	1.17 ± 0.06	231.73	376.57	502.09	372 ± 175
DEE4	88	0.03	1.0	1.28 ± 0.02	178.54	297.56	426.51	311 ± 170
DEE2C	80	0.02	1.0	1.20 ± 0.02	70.35	117.15	163.94	128 ± 77
DEE3C	82	0.07	1.0	1.32 ± 0.06	118.80	201.79	284.78	208 ± 111
DEE4C	88	0.01	1.0	1.35 ± 0.01	127.36	199.00	262.68	190 ± 100

**Values of X_i (μm) are related to the pore-size distribution and mean that i % of the pores have diameters lower than X $\mu\pi\iota$ (see text for details).*

Analysis of results shows the following general trends that are valid for both organic and carbon foams:

1. Total porosity increases from DEE2 to DEE4.
2. Closed porosity is almost negligible for all foams.
3. For the three kinds of foams, all pores are interconnected.
4. Tortuosity increases, on average, from DEE2 to DEE4.
5. Pore-size distribution broadens from DEE2 to DEE3 and DEE4; however, if the mean pore size is markedly shifted to higher values from DEE2 to DEE3 or DEE4, it is not so clear from DEE3 to DEE4; the medians of the distributions are rather similar, despite the corresponding different densities.

After carbonization, the following trends are observed:

1. Porosity decreases.
2. Pore-size distributions are shifted toward lower values compared to those of the starting organic foams.
3. Connectivity is not affected by carbonization.
4. Tortuosity tends to increase after carbonization.

Porosity

Even though the evolution of porosity with the synthesis conditions follows the expected trend, the values given in Table 2 are typically 10% lower than what is straightforwardly calculated from bulk density measurements and helium pycnometry Total and closed porosity measured according to the methods described for porosity determination above are given in Table 3, as well as average pore sizes determined from SEM pictures. As explained in the image analysis methods, this difference could come from the remaining noise on the images, due to the adopted image processing. However, as proven by SEM pictures, this disagreement can be more likely attributed to the contribution of pores having sizes lower than the pixel size of the image obtained with the microtomograph, i.e., lower than 4 μm.

Indeed, SEM images may partly account for this assumption through the direct observation of the narrow, open, porosity whereas very small closed cells were only revealed by pycnometry of crushed materials. Moreover, the discrepancy between results of helium pycnometry and microtomography could not be ascribed to neither spatial inhomogeneity of samples nor to a lack of repeatability.

Figure 5 shows a micrograph of the surface of a DEE4C sample. Figure 5a was obtained with secondary electrons so the topological contrast is best seen, whereas Figure 5b is the same picture but obtained with backscattered electrons, best showing the chemical contrast. These complementary images are of interest because cells and pore walls are well defined in Figure 5a, whereas holes and cell windows are more clearly discernible in Figure 5b. Each ring drawn in Figure 5b encircles at least one hole having a diameter equal or lower than 4 μm, hence not detected by microtomography. Such small, open pores are all over the surface, so it can be expected that they are also present in the volume, located within the struts of the foam structure. Moreover, pores more or less closed by thin membranes are seen on several SEM images (Fig. 5a). Such pore walls have thicknesses far below the resolution of the microtomograph (see Fig. 5d).

Therefore, narrow pores detected by pycnometry (Table 3) and SEM, and closed pores observed by SEM, might account for the 10% of lacking total porosity as well as the random noise remaining after image processing.

Table 3. *Pore Structure Parameters Derived from Helium Pycnometry and Analysis of SEM Images.*

Sample	Total Porosity (%)	Closed Porosity (%)	Average Pore Diameter *(μm)*
DEE2	93.9	6.5	220
DEE3	95.8	5	260
DEE4	96.7	4.5	280
DEE2C	94.2	7	195
DEE3C	96	6	240
DEE4C	96.6	5.5	255

Connectivity and Tortuosity

According to the underestimation of total and closed porosity, related properties such as connectivity and tortuosity are expected to be inaccurate: overestimated and underestimated, respectively. However, the values gathered in Table 2 are totally consistent with what can be deduced from a simple foam model based on a close packing of identical spherical pores. This suggests that tortuosity and connectivity are controlled by the larger pores. Indeed, for a face-centered cubic (FCC) packing, the tortuosity should lie between 1 and $\sqrt{2} = 1.41$, whereas it ranges from 1 to $\sqrt{3}/\sqrt{2} = 1.22$ for a hexagonal close compact (HCC) packing (see Fig. 6).

Table 2 shows that, even if the effect is low, tortuosity tends to decrease when the density increases. Such a finding is consistent with the pore-size distributions also derived from microtomography and given in Figure 2, which broadens when the density decreases. Such decrease of uniformity in the cell diameters probably induces the corresponding low increase of tortuosity.

Physical Properties Derived from Microtomography Studies: First Results

In the case of the present foams, presenting thin cell walls and a nonnegligible amount of pores smaller than the spatial resolution of a standard X-ray microtomograph, it could be concluded that the latter leads to somewhat inaccurate results. However, the smallest pores (some of them being closed) are not expected to control the properties of the materials, as far as fluid flow throughout the pore phase is concerned. Microtomograpic images with a pixel size of about 4 to 5 μm are important for characterizing such materials. Thus, typically 90% of the pore-size distribution is correct and especially the average pore size. Such data are of great interest for predicting the transport properties throughout the pore space of the materials as demonstrated by previous work (Knackstedt et al., 2006a, 2006b and references therein). Calculation of physical properties of the pore space based on the results given in the present article is in progress. The corresponding data will be compared with permeability, formation factor, and diffusivity measurements that are now being carried out. These studies should be published in the near future.

A few encouraging results based on the microtomography results have already been obtained, even without the use of complex computational simulations. The case of permeability of DEE3C material is considered here. A cubic sample was introduced in a close-fitting tube that was next filled with glue; the latter neither intruded the porosity nor covered the opposite faces of the cube through which water was forced to flow. The pressure drop ΔP and the flow rate of water throughout the sample Q were then measured, and the permeability k was calculated according to equation (3):

$$k = Q \frac{L}{S} \frac{n}{\Delta P}, \qquad (3)$$

where η is the dynamic viscosity of water at room temperature (10^{-3} Pa s), and L and S are the thickness and the cross-sectional area of the sample, respectively. The permeability was found to be $k \approx 2 \times 10^{-11}$ m^2.

From the data given in Table 2, similar permeability values can be recovered through the use of equations derived from the theory of Kozeny and Carman (Celzard et al., 2005 and references therein). These equations read:

$$k = \frac{\Phi (V_p / S_p)^2}{2T} \qquad (4)$$

and

$$k = \frac{\Phi^3}{\zeta S_{sp}^2}, \qquad (5)$$

where Φ is again the porosity, V_p (m^{3}g^{-1}) and S_p (m^{2}g^{-1}) are the volume and the surface of the open pore space per gram of material, respectively, T is the tortuosity, ζ is the Kozeny constant ($\zeta = 2$ for cylindrical tubes: not relevant here, $\zeta = 5$ in many materials), and S_{sp} (m^2 m^{-3}) = S_p/V_p is the internal accessible surface area per unit volume of solid material. Φ and T were taken from Table 2, ζ was assumed to be 5, and S_{sp} was calculated from the 3D microtomogra-phy images using the algorithm of the apparatus. For DEE3C, $S_{sp} = 100.8 \times 10^3$ m^{2}m^{-3}; using the apparent density given in Table 1, the calculated specific surface area of the material is 1.37 m^{2}g^{-1}, rather close to the one determined by nitrogen adsorption on the DEE4C sample, having a slightly lower density: 0.89 m^2 g^{-1} (Tondi et al., 2009).

Putting the aforementioned values of the parameters in equations (4) and (5), the calculated permeabilities are 1.09×10^{-11} m^2 and 3.06×10^{-11} m^2, respectively. Given the limitation of Kozeny-Carman's theory, which best describes the behavior of a bundle of cylindrical, parallel, and tortuous tubes, these results may be considered as very satisfactory. The permeabilities of more samples now need to be measured, and more accurate theories like those of Katz and Thompson or Johnson, Koplik, and Schwartz (Celzard & Marêché, 2001, 2002; Celzard et al., 2002) should be tested, as well as computations based on the lattice-Boltzmann method (Qian et al., 1992; Martys & Chen, 1996).

Published in : Microscopy and Microanalysis (2009), vol.15, pp. 384-394
Status: Postprint (Author's version)

Figure 4. *Pore-size distribution of (a) organic and (b) carbonized foams.*

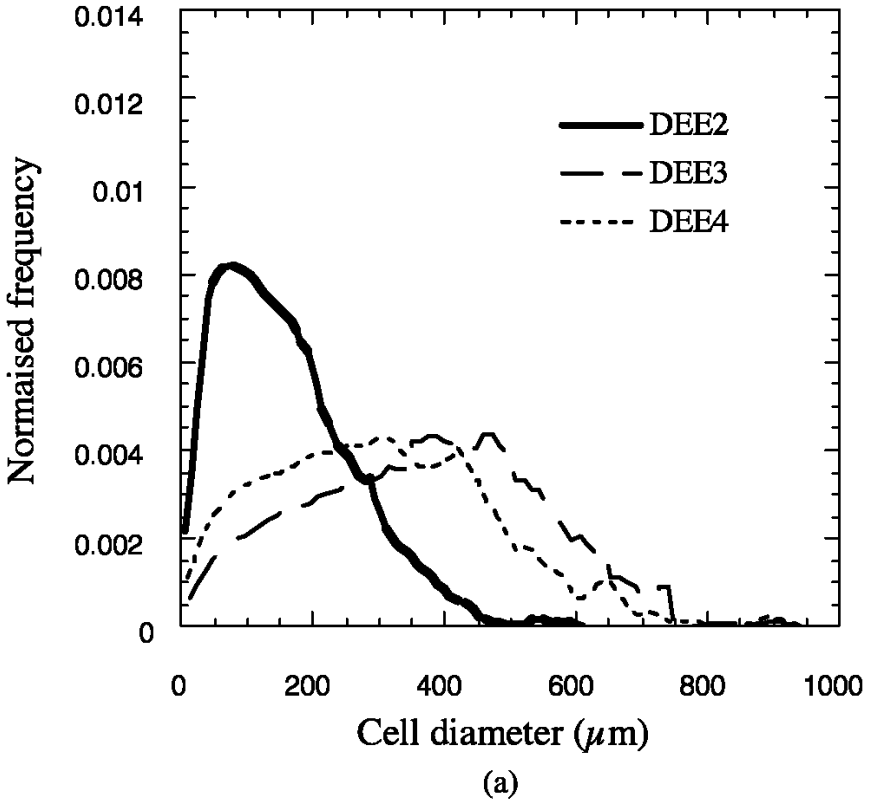

(a)

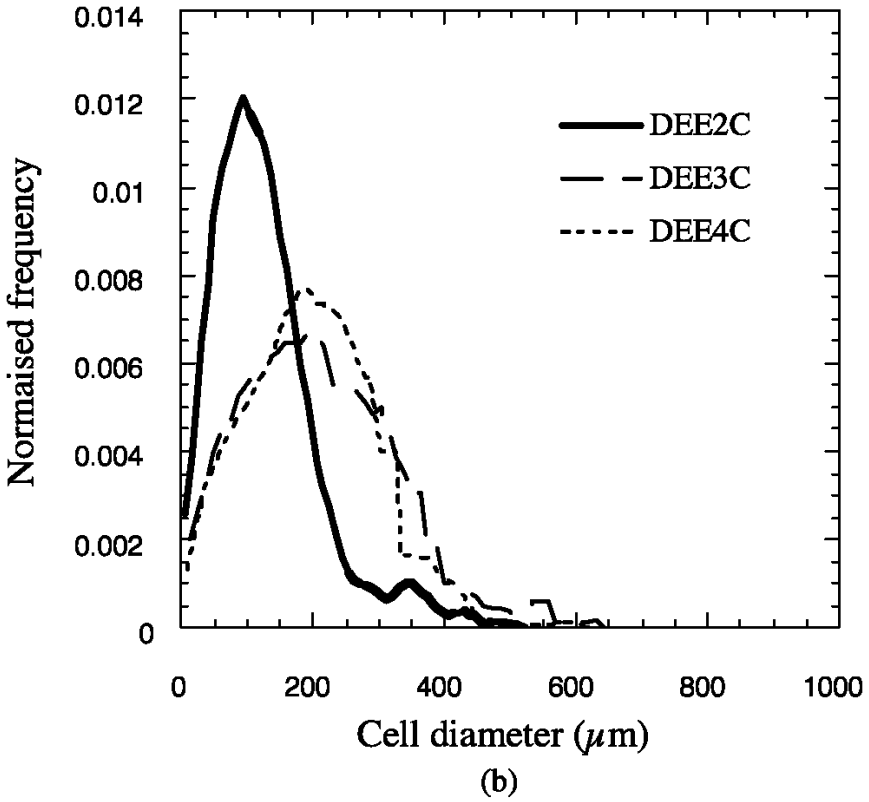

(b)

Published in : Microscopy and Microanalysis (2009), vol.15, pp. 384-394
Status: Postprint (Author's version)

Figure 5. *SEM pictures of DEE4C foam: (a) secondary electron image, (b) same as (a) but obtained with backscattered electrons, and (c) same as (b) at higher magnification. (d) High magnification secondary image showing thin, torn cell membranes. Circles indicate the presence of pores narrower than 4 μιη; the arrow shows a closed pore.*

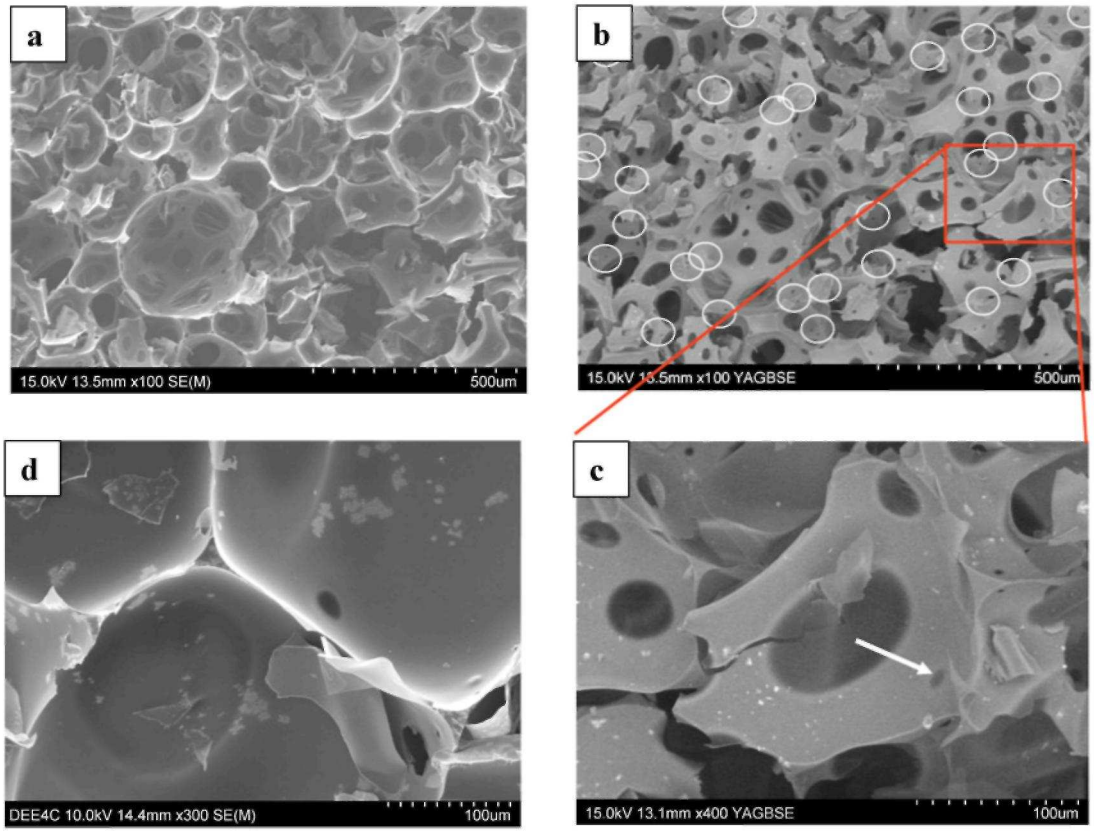

Figure 6. *Tortuosity in a close packing (see text) of spherical pores of radius r. (a) FCC packing; (b) HCC packing. The path represented by the plain arrow is √2 and √3/ √2 longer than the one pictured by the dotted arrow for FCC and HCC packing, respectively.*

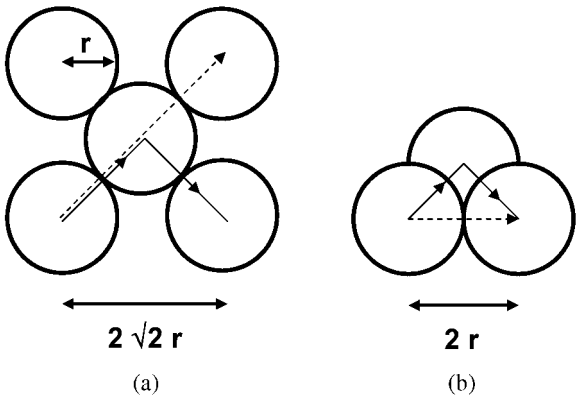

CONCLUSION

Pore structure is a key characteristic of foams that must be determined to understand their function and applications. In this work, X-ray microtomography coupled with image analysis was used to characterize the pore structure of tannin-based foams and their carbonized counterparts. The main advantages of this technique are its nondestructive character and its ability to quantify the 3D arrangement of the investigated object.

Extremely useful parameters such as pore-size distribution and tortuosity were derived, taking into account that objects with size below 4 µm could not be imaged, regarding the characteristics of the used microtomograph. From these data, prediction of physical properties should be possible, and a first very encouraging result was obtained with permeability. Parameters such as connectivity and total and closed porosity were shown to be less accurate with a higher resolution being needed. However, the method proved to be suitable for comparing a series of homologous materials. The following trends were thus observed when the density of the organic foam increases: narrowing of the pore-size distribution, shift of its center toward lower values, and decrease of both porosity and tortuosity.

Carbon foams obtained by pyrolysis of the organic materials were seen to present a similar pore structure, on average, except the following trends induced by carbonization: narrower pore-size distribution, smaller cells, and slightly higher tortuosity. All these data would have been difficult to obtain using only SEM images.

Investigation of physical characteristics and properties such as permeability and diffusivity (both related to open porosity and tortuosity) and surface area (related to pore diameter and pore volume) is in progress. From such studies, cross-property relationships can be derived similar to those described in Celzard et al. (2003), and comparing measurements with results of numerical computations can be systematically carried out.

ACKNOWLEDGMENTS

A. Léonard is grateful to the FRS-FNRS (Belgian Fund for Scientific Research) for her Research Associate position. A. Celzard gratefully acknowledges the financial support of the CPER 2007-2013 "Structuration du Pôle de Compétitivité Fibres Grand'Est" (Competitiveness Fibre Cluster) through local (Conseil Général des Vosges), regional (Région Lorraine), national (DRRT and FNADT), and European (FEDER) funds.

REFERENCES

BABIN, P., DELLA VALLE, G., DENDIEVEL, R., LOURDIN, D. & SALVO, L. (2007). X-ray tomography study of the cellular structure of extruded starches and its relations with expansion phenomenon and foam mechanical properties. *Carbohyd Polym* 68, 329-340.

BLACHER, S., LÉONARD, A., HEINRICHS, B., TCHERKASSOVA, N., FERAUCHE, R, CRINE, M., MARCHOT, P., LOUKINE, E. & PIRARD, J.P. (2004). Image analysis of X-ray microtomograms of Pd-Ag/ $Si0_2$ xerogel catalysts supported on $A1_20_3$ foams. *Colloid Surface A* 241, 201-206.

CELZARD, A., COLLAS, F., MARÊCHÉ, J.F., FURDIN, G. & REY, I. (2002). Porous electrodes-based double-layer supercapacitors: Pore structure vs series resistance.*J Power Sources* 108, 153-162.

CELZARD, A. & MARÊCHÉ, J.R (2001). Permeability and formation factor of compressed expanded graphite, *J Phys Condens Matter* 13, 4387-4403.

CELZARD, A. & MARÊCHÉ, J.R (2002). Fluid flow in highly porous anisotropic graphites. *f Phys Conde.ns Matter* 14, 1119-1129.

CELZARD, A., MARÊCHÉ, J.R & FURDIN, G. (2003). Describing the properties of compressed expanded graphite through power laws. *] Phys Condens Matter* 15, 7213-7226.

CELZARD, A., MARÊCHÉ, J.R & FURDIN, G. (2005). Modelling of exfoliated graphite. *Prog Mater Sci* 50, 93-179.

CLENNELL, M.B. (1997). Tortuosity: A guide through the maze. *Geol Soc Special Pub* 137, 113-127.

GIBSON, L.J. & ASHBY, M.R (1997). *Cellular Solids: Structure and Properties*, 2nd ed. Cambridge, UK: Cambridge University Press.

GOMMES, C.J., BONS, A.J., BLACHER, S., DUNSMUIR, J.H. & Tsou, A.H. (2009). Practical methods for measuring the tortuosity of porous materials from binary or grey-tone tomographic reconstructions. *AICHE J* 55, 2000-2012.

KAK, A.C. & SLANEY, M. (1988). *Principles of Computerized Tomographic Imaging*. New York: IEEE Press Inc.

KNACKSTEDT, M.A., ARNS, C.A., SAADAFTAR, M., SENDEN, T.J., LiMAYE, A., SAKELLARIOU, A., SHEPPARD, A.P., SOK, R.M., SCHROF, W. & STEININGER, H. (2006a). Elastic and transport properties of cellular solids derived from three-dimensional tomographic images. *Proc R Soc A* 462, 2833-2862.

KNACKSTEDT, M.A., ARNS, C.A., SENDEN, T.J. & GROSS, K. (2006b). Structure and properties of clinical coralline implants measured via 3D imaging and analysis. *Biomaterials* 27, 2776-2786.

KOHLER, R. (1981). A segmentation system based on thresholding. *Comput Graphics Image Proc* 15, 319-338.

LÉONARD, A., BLACHER, S., NiMMOL, C. & DEVAHASTIN, S. (2008a). Effect of far-infrared radiation assisted drying on microstructure of banana slices: An illustrative use of X-ray microtomog-raphy in microstructural evaluation of a food product. *J Food Eng* 85, 154-162.

LÉONARD, A., CALBERG, C, KERCKHOFS, G., WEVERS, M., JÉRÔME, R., PIRARD, J.P., GERMAIN, A. & BLACHER, S. (2008b). Characterization of the porous structure of biodegradable scaffolds obtained with supercritical $C0_2$ as foaming agent. *J Porous Mat* 15, 397-403.

MAIRE, E., COLOMBO, P., ADRIEN, J., BABOUT, L. & BIASETTO, L. (2007). Characterization of the morphology of cellular ceramics by 3D image processing of X-ray tomography. *J Eur Ceram Soc* 27, 1973-1981.

MAQUET, V., BLACHER, S., PIRARD, R., PIRARD, J.P., VYAKARNAM, M.N. & JÉRÔME, R. (2003). Preparation of macroporous biodegradable poly(L-lactide-co-ε-caprolactone) foams and characterization by mercury intrusion porosimetry, image analysis, and impedance spectroscopy. *J Biomed Mater Res A* 66, 199-213.

MARTYS, N.S. & CHEN, H. (1996). Simulation of multicomponent fluids in complex three-dimensional geometries by the lattice Boltzmann method. *Phys Rev E* 53, 743-750.

MEIKLEHAM, N.E. & Pizzi, A. (1994). Acid- and alkali-catalyzed tannin-based rigid foams. *J Appl Polym Sci* 53, 1547-1556.

PIZZI, A. (1994). *Advanced Wood Adhesives Technology*. New York: Marcel Dekker.

QIAN, Y.H., D'HUMIERES, D. & LALLEMAND, P. (1992). Diffusion simulation with a deterministic one-dimensional lattice-gas model. *J Stat Phys* 68, 563-573.

RUSS, J.C. (1999). *The Image Processing Handbook*, 2nd ed. Boca Raton, FL: CRC Press.

SOILLE, P. (1999). *Morphological Image Analysis. Principles and Applications.* Berlin, Germany: Springer.

TIJA, J. & MOGHE, P.J. (1998). Analysis of 3-D microstructure of porous poly(lactide-glycolide) matrices using confocal micros-copy. *J Biomed Mater Res A* 43, 291-299.

TONDI, G., FIERRO, V., Pizzi, A. & CELZARD, A. (2009). New tannin-based carbon foam. *Carbon* 47, 1480-1492; doi:10.1016/ j.carbon.2009.01.041.

TONDI, G., Oo, C.W., Pizzi, A., TROSA, A. & THEVENON, M.F. (2008a). Metal adsorption of tannin based rigid foams. *Ind Crops Prod* 29, 336-340; doi:10.1016/j.indcrop.2008.06.006.

TONDI, G. & Pizzi, A. (2008). Tannin-based rigid foams: Characterization and modifications. *Ind Crops Prod* 29, 356-363; doi: 10.1016/j.indcrop.2008.07.003.

TONDI, G., PIZZI, A. & OLIVES, R. (2008b). Natural tannin-based rigid foams as insulation for doors and wall panels. *Maderas Ci Tecnol* 10, 219-227.

TRATER, A.M., ALAVI, S. & Rizvi, S.S.H. (2005). Use of noninvasive X-ray microtomography for characterizing microstructure of extruded biopolymer foams. *Food Res Int* 38, 709-719.

VAN LENTHE, G.H., HAGENMÜLLER, H., BOHNER, M., HOLLISTER, S.J., MEINEL, L. & MÜLLER, R. (2007). Nondestructive micro-computed tomography for biological imaging and quantification of scaffold-bone interaction *in vivo*. *Biomaterials* 28, 2479-2490.

VIOT, P., PLOUGONVEN, E. & BERNARD, D. (2008). Microtomography on polypropylene foam under dynamic loading: 3D analysis of bead morphology evolution. *Compos Part A-Appl S*, 39, 1266-1281.